Magnetotransport Properties of Cd_3As_2 Nanostructures

Enze Zhang,[†,‡,#] Yanwen Liu,[†,‡,#] Weiyi Wang,[†,‡] Cheng Zhang,[†,‡] Peng Zhou,[§] Zhi-Gang Chen,*[,∥] Jin Zou,*[,∥,⊥] and Faxian Xiu*[,†,‡]

[†]State Key Laboratory of Surface Physics and Department of Physics, Fudan University, Shanghai 200433, China, [‡]Collaborative Innovation Center of Advanced Microstructures, Fudan University, Shanghai 200433, China, [§]State Key Laboratory of ASIC and System, Department of Microelectronics, Fudan University, Shanghai 200433, China, [∥]Materials Engineering, The University of Queensland, Brisbane, QLD QLD 4072, Australia, and [⊥]Centre for Microscopy and Microanalysis, The University of Queensland, Brisbane, QLD 4072, Australia. [#]These authors contributes equally to this work.

ABSTRACT Three-dimensional (3D) topological Dirac semimetal has a linear energy dispersion in 3D momentum space, and it can be viewed as an analogue of graphene. Extensive efforts have been devoted to the understanding of bulk materials, but yet it remains a challenge to explore the intriguing physics in low-dimensional Dirac semimetals. Here, we report on the synthesis of Cd_3As_2 nanowires and nanobelts and a systematic investigation of their magnetotransport properties. Temperature-dependent ambipolar behavior is evidently demonstrated, suggesting the presence of finite-size of bandgap in nanowires. Cd_3As_2 nanobelts, however, exhibit metallic characteristics with a high carrier mobility exceeding 32 000 $cm^2 V^{-1} s^{-1}$ and pronounced anomalous double-period Shubnikov-de Haas (SdH) oscillations. Unlike the bulk counterpart, the Cd_3As_2 nanobelts reveal the possibility of unusual change of the Fermi sphere owing to the suppression of the dimensionality. More importantly, their SdH oscillations can be effectively tuned by the gate voltage. The successful synthesis of Cd_3As_2 nanostructures and their rich physics open up exciting nanoelectronic applications of 3D Dirac semimetals.

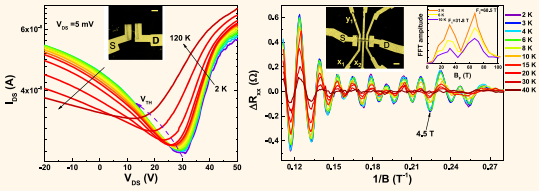

KEYWORDS: nanowire · ambipolar effect · nanobelt · Shubnikov-de Haas oscillations · gate tunability

Dirac materials like graphene and topological insulators have been widely studied in recent years owing to their exciting physical properties originated from two-dimensional (2D) Dirac Fermions.[1−5] In contrast with conventional semiconductors, their band structures obey a linear energy dispersion relation and possess vanishing effective mass near the Dirac point, thus promising applications in optoelectronics[6−9] and spintronics.[10−12] Recently, theory predicts the existence of three-dimensional (3D) Dirac Fermions where the Dirac nodes are developed *via* the point contact of conduction-valence bands. The potential candidates involve β-BiO_2, Na_3Bi, and Cd_3As_2.[13−15] Interestingly, these 3D topological Dirac semimetals can be driven into topological insulators[14] or Weyl semimetals[14,16,17] by breaking symmetries that may lead to the discovery of novel physical phenomena such as quantum spin Hall effect and topological superconductivity.[14] Soon after the theoretical predictions, experiments like angle-resolved photoemission spectroscopy (ARPES)[3,18−20] and scanning tunneling microscopy[21] were carried out on Na_3Bi and Cd_3As_2 to investigate the 3D Dirac Fermions.

Cd_3As_2 has been paid special attention due to its chemical stability in air and extremely high mobility at both low and room temperatures.[20,22] Studies based on Cd_3As_2 bulk materials have shown ultrahigh mobility of 9×10^6 $cm^2 V^{-1} s^{-1}$ at 5 K[23] and up to 1.5×10^4 cm^2 V^{-1} s^{-1} at room temperature.[22] Giant and linear magnetoresistance[23,24] and nontrivial π Berry's phase[25] of Dirac Fermions were demonstrated in transport experiments. Recently, a superconductivity phase was also identified in a Cd_3As_2 crystal making it an interesting candidate of the topological superconductors.[26−29] However, despite the extensive studies on Cd_3As_2 bulk materials, few efforts have been devoted to the low-dimensional nanostructures, such as nanowires[30,31] or nanobelts.

In this article, we present the magnetotransport properties of Cd_3As_2 nanostructures. The superb crystallinity of as-grown Cd_3As_2 nanowires allows us to observe the semiconductor-like ambipolar effect, indicating the band gap opening. In contrast, Cd_3As_2 nanobelts exhibit high carrier mobility

* Address correspondence to faxian@fudan.edu.cn, j.zou@uq.edu.au, z.chen1@uq.edu.cn.

Received for review April 15, 2015 and accepted August 22, 2015.

Published online August 24, 2015
10.1021/acsnano.5b02243

and pronounced double-period Shubnikov-de Haas (SdH) oscillations that can be effectively modulated by applied back-gate voltage (V_{BG}). The reduced dimensionality in these nanostructures, compared with the bulk crystals, offers the artificial suppression of Fermi sphere, thus allowing for the observation of unique magnetotransport properties.

RESULTS AND DISCUSSION

Transmission electron microscopy (TEM) was carried out to determine the structural characteristics of the synthesized Cd_3As_2 nanostructures. Figure 1a is a TEM image of a typical Cd_3As_2 nanowire with a diameter of ~80 nm. Figure 1b is a selected area electron diffraction (SEAD) pattern. The combination of panels a and b of Figure 1 indicates that the Cd_3As_2 nanowire is grown along [112] direction. The corresponding high-resolution (HR) TEM is depicted in Figure 1c, which clearly shows the d_{112} spacing of 7.3 Å. Figure 1d displays another type of the Cd_3As_2 nanostructures—nanobelts—with an axial direction along [110], confirmed by the SAED pattern (Figure 1e), from which the large smooth surface of the nanobelt can be indexed as (112). The corresponding high-resolution (HR) TEM is shown in Figure 1f, which clearly shows the d_{110} spacing of 4.6 Å.

To fabricate a field effect transistor (FET), the Cd_3As_2 nanowires were transferred onto a prepatterned SiO_2/Si substrate. Optical microscopy and scanning electron microscopy (SEM) were subsequently used to locate the nanowires and determine their diameters. Source/Drain contacts were then deposited *via* a standard electron-beam lithography (EBL) process. Figure 2a (inset) shows the schematic drawing of the two-terminal FET device with an ~40 nm-diameter Cd_3As_2 nanowire on top of a 285 nm SiO_2 gate (also see the SEM image, inset of Figure 2b). A V_{BG} was applied on the degenerated silicon substrate to modulate the channel conductance. The gate-tuned source-drain current (I_{DS}) varies linearly with source-drain voltage (V_{DS}), indicating an Ohmic behavior (Figure 2a). A typical temperature-dependent resistance of the nanowires shows semiconducting characteristics (Figure 2b), indicative of a band gap opening[30,32] which is reminiscent of that in graphene nanoribbons.[33,34] The activation energy can be further acquired by fitting the high-temperature resistance to equation $R_{xx} \sim \exp(E_a/k_BT)$, where E_a is the activation energy and k_B is the Boltzmann constant (Figure 2b inset). Here, E_a is extracted to be ~30 meV and the band gap E_{gap} of the nanowire can be roughly estimated to be over 60 meV. To examine the temperature-dependent switching behavior of the Cd_3As_2 nanowire FET, the transfer curves of the device were obtained by sweeping V_{BG} under a certain V_{DS} of 5 mV from 2 to 120 K (Figure 2c). A strong ambipolar behavior is observed. The dashed guiding line in Figure 2c shows the shift of the threshold voltage V_{TH} toward the negative direction as temperature increases. This is originated from the increasing electron charge carriers in the channel at elevated temperatures. Additionally, the shift of the minimum conduction point to the positive direction at certain temperatures indicates the presence of interface charges between the Cd_3As_2 nanowire and SiO_2.[35] Moreover, temperature-dependent electron and hole mobility can be extracted from the linear region of the transfer characteristics using the equation,[36−38]

$$\mu_{FE} = [dI_{DS}/dV_{BG}] \times [L^2/(C_{ox}V_{DS})] \quad (1)$$

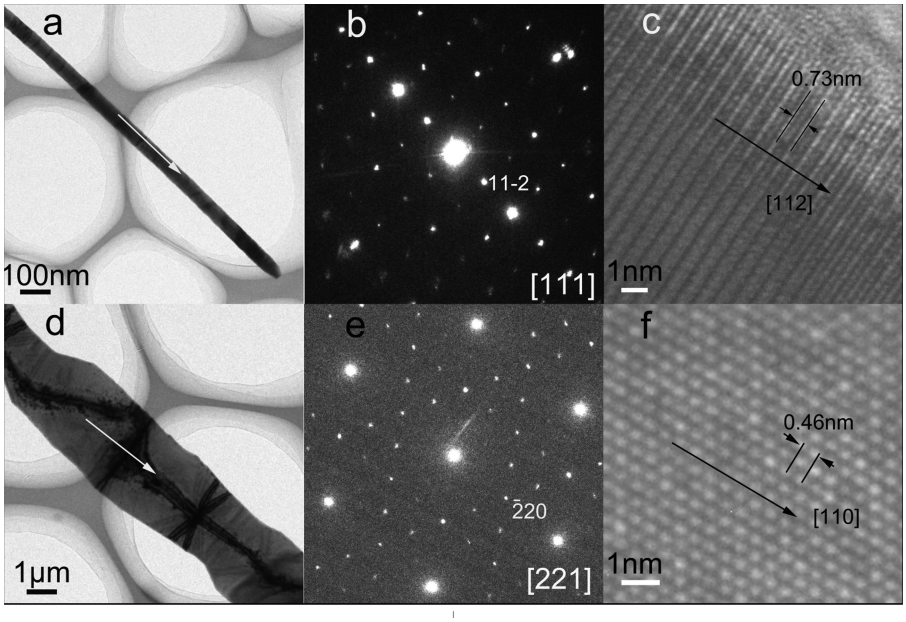

Figure 1. Microstructural characteristics of Cd_3As_2 nanostructures. (a) TEM, (b) SEAD, and (c) HRTEM images of the typical Cd_3As_2 nanowire; (d) TEM, (e) SEAD, and (f) HRTEM images of the typical Cd_3As_2 nanobelt.

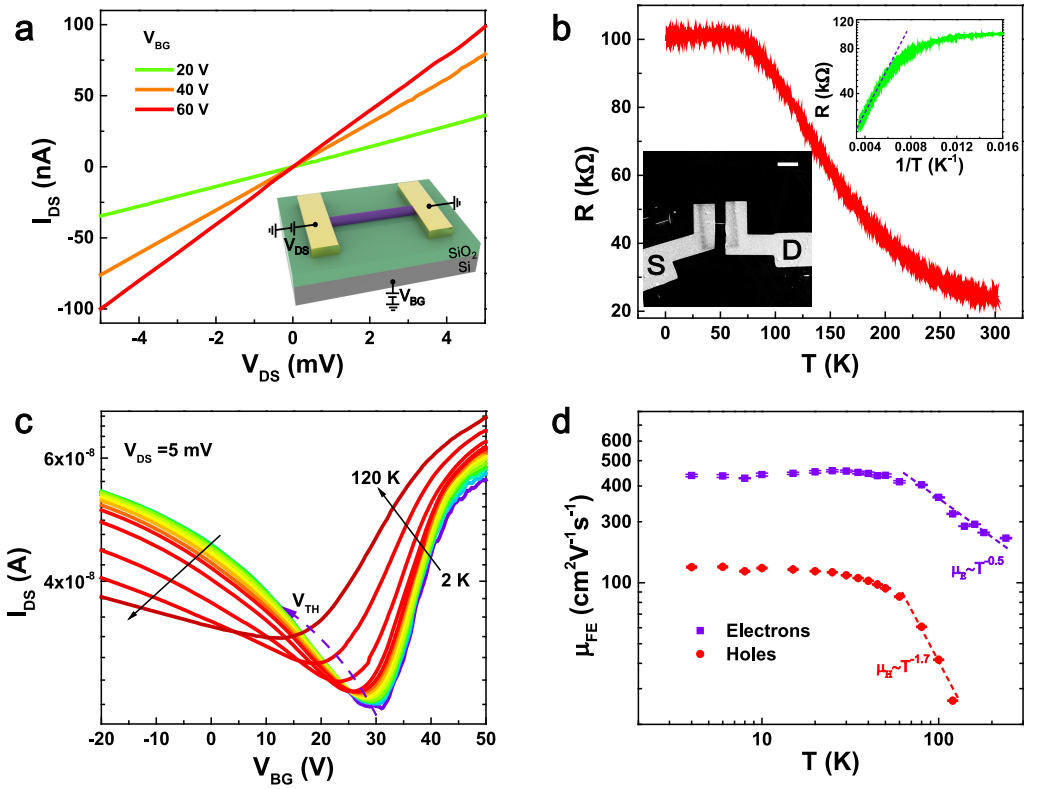

Figure 2. Cd_3As_2 nanowire field-effect transistor (FET) and its device characteristics. (a) The output characteristics ($I_{DS}-V_{DS}$) of the device under different back-gate voltages at 2 K. The inset shows a schematic structure of the fabricated device. (b) Typical channel resistance *versus* temperature ($R-T$) under zero back-gate voltage. The inset shows a SEM image of the FET device. Scale bar, 5 μm. (c) Temperature-dependent transfer curves of the device showing ambipolar effect at a fixed V_{DS} = 5m V. (d) Field-effect mobility of electrons and holes as a function of temperature on a logarithmic scale.

where dI_{DS}/dV_{BG} is the slope of the transfer curve in the linear regime, L is the channel length, and $C_{ox} = (2\pi\varepsilon_0\varepsilon L)/[\cosh^{-1}(r + t_{ox}/r)]$ is the capacitance between the channel and the back gate through the SiO_2 gate dielectric (ε_r = 3.9; t_{ox} = 285 nm; r is the radius of the Cd_3As_2 nanowire). As shown in Figure 2d, the mobility reaches the maximum value at ~20 K and decreases as temperate is increased which is attributed to the electron−phonon scattering.[39] The temperature dependence of mobility typically follows the relation $\mu \propto T^{-\gamma}$, where the temperature damping factor γ depends on electron−phonon coupling in the nanowire channel. When we perform the best fit to the linear part of the curves (dash lines in Figure 2d), γ can be obtained to be ~0.5 and 1.7 for electrons and holes, respectively. Further suppression of phonon scattering can be realized by encapsulation of the nanowire in high-κ dielectric environment.[40]

Nanobelt is another form of nanostructures to study the physics in Cd_3As_2. To investigate the magnetotransport properties of the Cd_3As_2 nanobelts, back-gate devices with a standard Hall-bar geometry were fabricated, as schematically illustrated in Figure 3a (also see the SEM image, inset of Figure 3b). The longitudinal resistance (R_{xx}) as a function of temperature ($R_{xx}-T$) at zero magnetic field is acquired from the device with a 120 nm-thick Cd_3As_2 nanobelt (device 01, Figure 3b). Clearly, it shows a metallic behavior that is different from amorphous semiconducting Cd_3As_2 thin films.[41] In contrast with the quantum confinement effect in nanowires (gap opening), the Cd_3As_2 nanobelts are thick enough to incur the widely observed band inversion (gapless),[14] leading to the high mobility and metallic characteristics. Figure 3c depicts the electron Hall slopes at different temperatures, from which the temperature-dependent Hall mobility and carrier density can be extracted (Figure 3d). The mobility reaches up to 32 000 $cm^2\ V^{-1}\ s^{-1}$ and drops as temperature rises because of the enhanced electron−phonon scattering.[40] By fitting the linear part of the curve (dash line in Figure 3 d) to the power law $\mu \propto T^{-\gamma}$, $\gamma \sim 0.5$ can be obtained. We also observed a clear Hall anomaly and attribute it to the crystal anisotropy at low temperatures which is consistent with former transport experiments of Cd_3As_2 bulk materials.[23]

Owing to the high mobility of electrons in Cd_3As_2 nanobelts, we were able to resolve the SdH oscillations in the longitudinal magnetoresistance (R_{xx}) of the samples. Figure 4a displays the vertically shifted R_{xx} as a function of magnetic field B at different temperatures. Surprisingly, pronounced double-period SdH oscillations persist up to 40 K. When the background is subtracted, the plots of oscillation amplitude ΔR_{xx} *versus* 1/B from 2 to 40 K can be obtained, as depicted

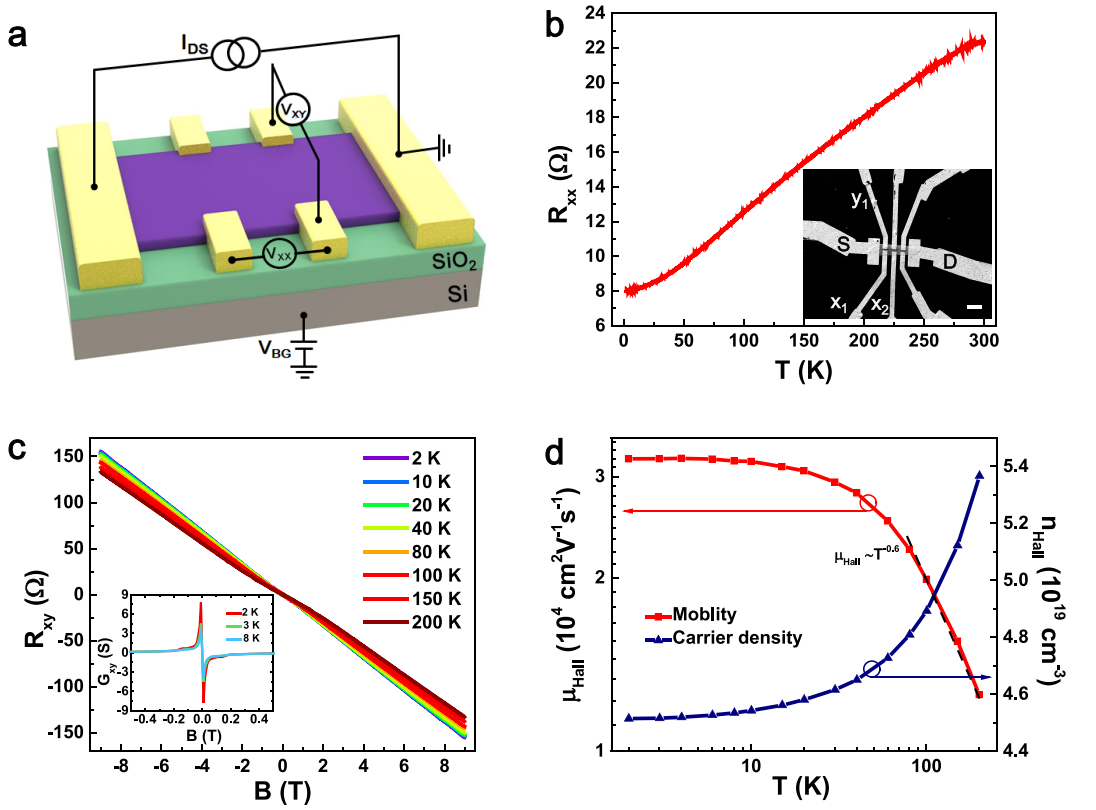

Figure 3. Cd_3As_2 nanobelt Hall-bar device and Hall effect characteristics. (a) Schematic device structure. (b) R_{xx} as a function of temperature (R_{xx}–T) at zero magnetic field. The inset shows a SEM image of the device. Scale bar, 5 μm. (c) Hall resistance obtained at different temperatures. The inset shows a Hall anomaly of the device at low temperatures. (d) Hall mobility and carrier density deduced from the Hall slopes.

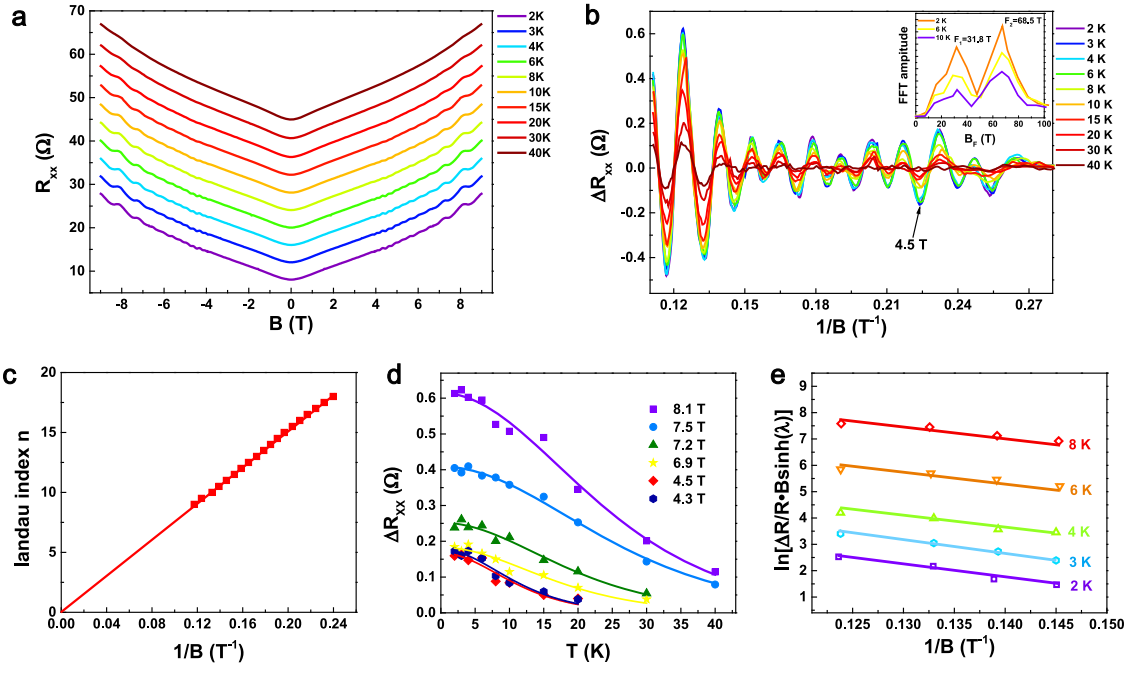

Figure 4. Temperature-dependent SdH oscillations of the Cd_3As_2 nanobelt Hall bar device. (a) Vertically shifted R_{xx} as a function of B obtained at different temperatures showing two frequencies. (b) Temperature-dependent SdH oscillations' amplitude ΔR_{xx} as a function of 1/B after subtracting the background from (a). Inset: FFT of SdH oscillation with two frequencies F_1 = 31.8 T, F_2 = 68.5 T. (c) Landan fan diagram for SdH oscillations. The intercept is 0.32, which attributes to the trivial state. (d) ΔR_{xx} as a function of temperature from which the effective cyclotron mass $m_{cyc} = 0.046m_e$ can be determined. (e) Dingle plots for the extraction of quantum lifetime.

TABLE 1. Estimated Parameters from the SdH Oscillations

device label	V_G(V)	F_{SdH} (T)	S_f(10^{-3} Å^{-2})	K_f (Å)	m_{cyc}(m_e)	V_F(10^6m/s)	E_f(meV)	t (10^{-13} s)	l (nm)	μ_{SdH}(cm^2 V^{-1} s^{-1})
01	0	68.5	6.53	0.046	0.046	1.16	352	1.59	184	6077

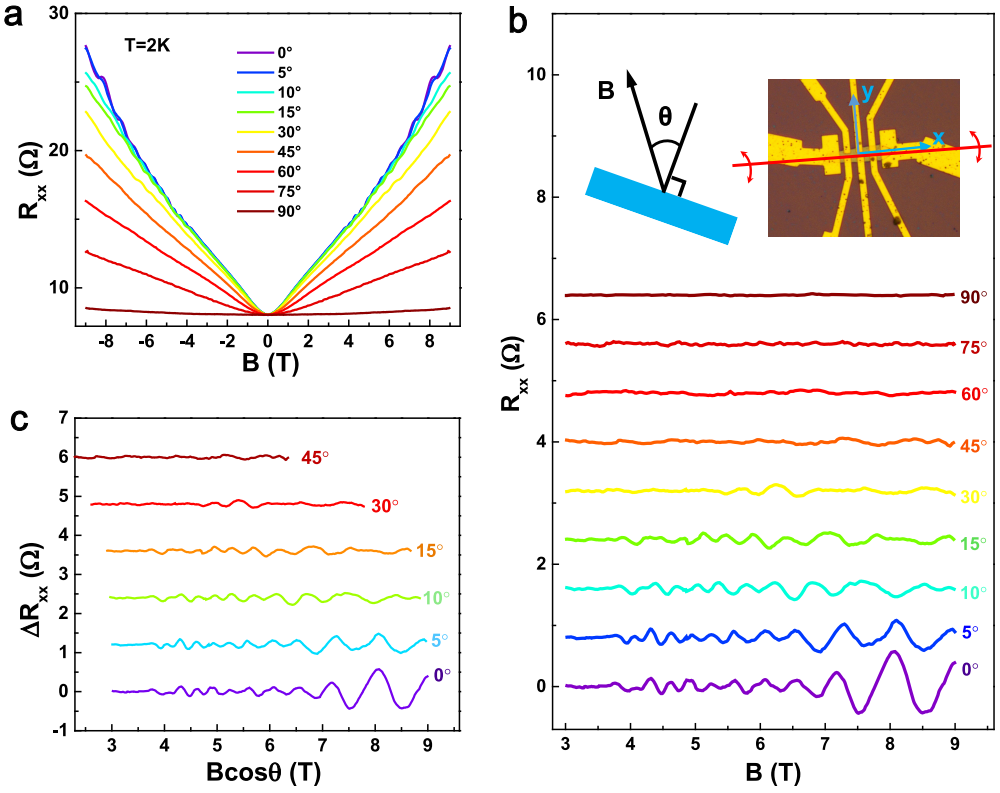

Figure 5. Angular-dependent SdH oscillations of the Cd_3As_2 nanobelt Hall bar device. (a) R_{xx} as a function of B at different tilt angle θ as defined in panel b inset. (b) SdH oscillations' amplitude ΔR_{xx} as a function of B after subtracting the background from (a). Inset: Measurement configuration; x and y indicate the crystal orientation of the Cd_3As_2 nanobelt. (c) SdH oscillations amplitude ΔR_{xx} as a function of B cos(θ).

in Figure 4b. With the increase of temperature, the oscillation amplitude drops rapidly.[25] The Landau fan diagram (Figure 4c) was plotted by taking the maximum and minimum of the oscillation amplitude ΔR_{xx} as the half integer and integer, respectively (Figure 4c).[42,43] The intercept is 0.32, which corresponds to a trivial Berry phase. Given the fact the Landau level is still far from the quantum limit, there may be some inaccuracy in the extrapolated intercept and further experiments can be done to address this. We note that the amplitude of the oscillations has a sudden increase when the magnetic field decreases to 4.5 T, suggesting two oscillation frequencies (Figure 4b). To obtain the oscillation frequencies F, we perform fast Fourier transformation (FFT) on the SdH oscillations; two distinct frequencies $F_1 = 31.8$ T and $F_2 = 68.5$ T can be obtained. By using the equation $F = (\phi_0/2\pi^2)S_F$, where $\phi_0 = h/2e$, two cross-section areas of the Fermi surface $S_{F1} = 6.53 \times 10^{-3}$ Å^{-2} and $S_{F2} = 3.03 \times 10^{-3}$ Å^{-2} can be acquired. During the experiments, we also confirm that the magnetic field B is perpendicular to (112) plane that causes the development of two nested ellipses in the cross section of Fermi surface, leading to the double-period anomalous SdH oscillations.[44−46] This is in a good agreement with previous ARPES results of two ellipsoidal Fermi surfaces.[18]

The observation of SdH oscillations is vital to analyze important parameters of the carrier transport.[47] To calculate the cyclotron mass (m_{cyc}), the temperature-dependent SdH oscillation amplitude ΔR_{xx} (Figure 4e) is extracted under zero back-gate voltage by fitting to the equation $\Delta R_{xx}(T)/R_{xx}(0) = \lambda(T)/\sinh(\lambda(T))$, where the thermal factor is given by $\lambda(T) = 2\pi^2 k_B T m_{cyc}/(\hbar e B)$, k_B is the Boltzmann's constant, $\hbar$ is the reduced plank constant and $m_{cyc} = E_F/v_F^2$ is the effective cyclotron mass. We can obtain the effective cyclotron mass $m_{cyc} = 0.046m_e$. Using the equation $v_F = \hbar k_F/m_{cyc}$, we can acquire the Fermi velocity $v_F = 1.16 \times 10^6$m/s and the Fermi energy $E_F = 352$ meV. Moreover, from the Dingle plot, the quantum lifetime τ time can be calculated from the Dingle factor exp($-D$), where $D = 2\pi^2 E_{Fc}/(\tau e B v_F^2)$. Since $\Delta R_{xx}(T)/R$ is propositional to $\exp(-D)\lambda(T)/\sinh(\lambda(T))$, we can find τ from the slope of the logarithmic plot of $\Delta R_{xx}(T)/R \sinh(\lambda(T))$ *versus* $1/B$.

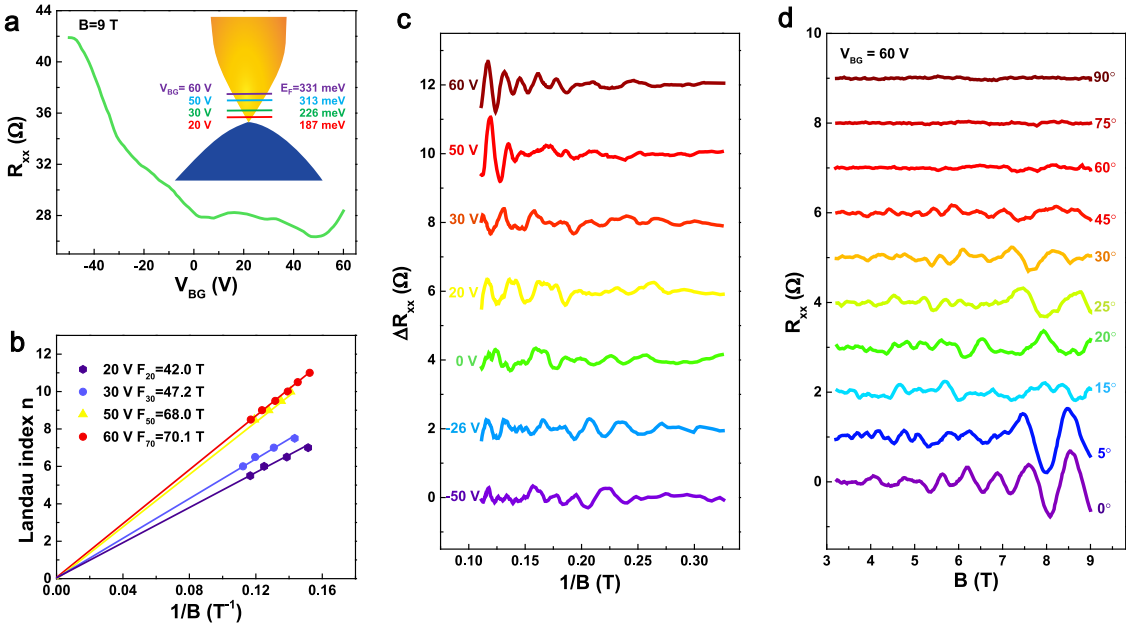

Figure 6. Gate-tuned SdH oscillations of the 80 nm-thick Cd_3As_2 nanobelt. (a) R_{xx} as a function of V_{BG} obtained at B = 9 T. Inset: Schematic band structure and the shifts of the Fermi level toward the conduction band at different V_{BG}. (c) Landan fan diagram of SdH oscillations for different V_{BG}. All the intercepts are around 0.3. (c) SdH oscillations amplitude ΔR_{xx} as a function of 1/B obtained at different V_{BG}. (d) Angular-dependent SdH oscillations amplitude ΔR_{xx} as a function of B at V_{BG} = 60 V.

With the use of extracted cyclotron masses, the quantum lifetime τ can be estimated to be 1.59×10^{-13} s.[4,48] Other important parameters such as mean free path $l = v_F\tau$ and the cyclotron mobility $\mu_{SdH} = e\tau/m_{cyc}$ are calculated, l = 184 nm, μ_{SdH} = 6077 $cm^2\ V^{-1}\ s^{-1}$, as summarized in Table 1.

To further probe the nature of SdH oscillations, the angular-dependent magnetotransport measurements were performed by tilting the sample from $\theta = 0°$ to 90°. Figure 5a depicts R_{xx} as a function of B at varying tilting angle θ, from which the SdH oscillations are observed to vanish when θ exceeds 45°. After subtracting the background, the oscillation amplitude as a function of B and B cos(θ) was plotted in Figure 5, panels b and c, respectively. It is known that for bulk Cd_3As_2 materials the SdH oscillations are observable from 0° to 90° owing to the nearly spherical Fermi surface,[23] while for the 2D electron gas in graphene or surface states in topological insulators, the SdH oscillations show unchanged peak positions in the B cos(θ) plot.[48,49] Our results, however, are distinctive to both scenarios. Considering the thickness of 120 nm of the nanobelt, the disappearance of SdH oscillations at $\theta > 45°$ is attributed to the highly anisotropic Fermi sphere.[13]

To examine the tunability of back-gate voltage to the SdH oscillations, magnetotransport measurements were also carried out on 80 nm-thick Cd_3As_2 nanobelts (device 02). Figure 6a illustrates R_{xx} as a function of back-gate voltage at 9 T. R_{xx} decreases with the increase of V_{BG}, showing a clear n-type behavior. Interestingly, the resistance shows an oscillation-like feature at the high V_{BG} regime, similar to that of 2D electron gas in black phosphorus.[50] Figure 6c illustrates the extracted SdH oscillations under different V_{BG} at 2 K. Under zero or negative gate bias, the magnetoresistance does not show well-resolved SdH oscillations. While by applying a positive V_{BG} of 20−60 V, pronounced SdH oscillations are obtained, suggesting the shifting of the Fermi level by back-gate voltage.[4,51,52]As showed in Figure 6b, the SdH oscillations' frequency increases from 42 to 70.1 T as V_{BG} varies from 20 to 60 V. The calculated Fermi energy increases from 187 to 331 meV, revealing the lifting of Fermi level further into the conduction band.[52] The angular-dependent SdH oscillations under 60 V were then examined and there are no observable SdH oscillations as θ goes beyond 45° (Figure 6d). This is consistent with the device measured under zero back-gate voltage. To further understand the SdH oscillations, the Berry's phase can be obtained from the Landau fan diagram (Figure 6b). According to the Lifshitz-Onsager quantization rule,[43]

$$A_F\frac{\hbar}{eB} = 2\pi\left(n + \frac{1}{2} - \frac{\Phi_B}{2\pi}\right) = 2\pi(n + 1/2 + \beta + \delta) \quad (2)$$

$2\pi\beta$ is Berry's phase, $2\pi\delta$ is the additional phase shift that changes from 0 for a quasi-2D cylindrical Fermi surface to $\pm$1/8 for a corrugated 3D Fermi surface.[25,43] In our Cd_3As_2 nanobelt samples, under different V_{BG} the intercept remains ~0.3, deviating from $\pm$1/8, indicating a trivial zero Berry's phase. The presence

of zero Berry's phase infers that the SdH oscillations mainly come from the high mobility conduction band and the Fermi surface is an anisotropic ellipsoid instead of sphere with prefect π Berry's phase.[44] It should be noted that with dimensionality reduced from bulk (3D) to nanowires (quasi-1D), Cd_3As_2 exhibits a transition from topological Dirac semimetal to trivial band insulator,[14] which makes the Dirac Fermions disappear due to the band gap opening. At this stage, the detailed band structure and exquisite physics of the Cd_3As_2 nanostructures deserve further theoretical investigations.

CONCLUSION

In summary, we have incorporated the 3D Dirac semimetal Cd_3As_2 nanostructures into field-effect devices including nanowire FET and nanobelt back-gated Hall bar devices. The FET device exhibits ambipolar behavior, reminiscence of narrow-band gap semiconductors. The gated-Hall bar devices, however, show ultrahigh mobility of Cd_3As_2 nanobelts and pronounced double-period SdH oscillations with reasonable gate tenability. Our results shed the light on the practical and versatile device applications of 3D Dirac semimetal in electronics.

METHODS

Growth of Cd_3As_2 Nanowires and Nanobelts. The samples were grown using Cd_3As_2 powders as precursors in a horizontal tube furnace, in which Argon was a carrier gas. The tube furnace was first pumped and flushed with argon gas in order to remove air. During the growth cycle, the tube furnace was ramped to the 760 °C within 15 min, held constant for 40 min, and cooled down naturally over ~2.5 h with a constant flow of argon. The precursor powder boat was placed in the hot center of the furnace, while the Si (100) substrates were placed downstream where the temperature was within the range from 200 to 400 °C

Device Fabrication and Measurement. The electrodes of the Cd_3As_2 nanowire FET devices and nanobelt Hall-bar device were fabricated by EBL using PMMA/MMA bilayer polymer. Cr/Au (5 nm/150 nm) electrodes were deposited by *e*-beam evaporation. The magnetotransport measurements of the devices were carried out in a Physical Property Measurement System (PPMS) system (Quantum design) using Agilent 2912 and lock-in amplifier SR830.

Conflict of Interest: The authors declare no competing financial interest.

Acknowledgment. This work was supported by the National Young 1000 Talent Plan, Pujiang Talent Plan in Shanghai, National Natural Science Foundation of China (61322407, 11474058), the Australian Research Council, and the QLD government for a smart state future fellowship (2011002414). Part of the sample fabrication was performed at Fudan Nanofabrication Laboratory.

Supporting Information Available: The Supporting Information is available free of charge on the ACS Publications website at DOI: 10.1021/acsnano.5b02243.

Additional results in Figures S1−S8 (PDF)

REFERENCES AND NOTES

1. Du, X.; Skachko, I.; Duerr, F.; Luican, A.; Andrei, E. Y. Fractional Quantum Hall Effect and Insulating Phase of Dirac Electrons in Graphene. *Nature* **2009**, *462*, 192–195.
2. Novoselov, K.; Geim, A. K.; Morozov, S.; Jiang, D.; Katsnelson, M.; Grigorieva, I.; Dubonos, S.; Firsov, A. Two-Dimensional Gas of Massless Dirac Fermions in Graphene. *Nature* **2005**, *438*, 197–200.
3. Chen, Y.; Analytis, J.; Chu, J.-H.; Liu, Z.; Mo, S.-K.; Qi, X.-L.; Zhang, H.; Lu, D.; Dai, X.; Fang, Z. Experimental Realization of a Three-Dimensional Topological Insulator, Bi_2Te_3. *Science* **2009**, *325*, 178–181.
4. Xiu, F.; He, L.; Wang, Y.; Cheng, L.; Chang, L. T.; Lang, M.; Huang, G.; Kou, X.; Zhou, Y.; Jiang, X.; Chen, Z.; Zou, J.; Shailos, A.; Wang, K. L. Manipulating Surface States in Topological Insulator Nanoribbons. *Nat. Nanotechnol.* **2011**, *6*, 216–21.
5. Peng, H.; Lai, K.; Kong, D.; Meister, S.; Chen, Y.; Qi, X.-L.; Zhang, S.-C.; Shen, Z.-X.; Cui, Y. Aharonov-Bohm Interference in Topological Insulator Nanoribbons. *Nat. Mater.* **2010**, *9*, 225–229.
6. Liu, C.-H.; Chang, Y.-C.; Norris, T. B.; Zhong, Z. Graphene Photodetectors with Ultra-Broadband and High Responsivity at Room Temperature. *Nat. Nanotechnol.* **2014**, *9*, 273–278.
7. Mueller, T.; Xia, F.; Avouris, P. Graphene Photodetectors for High-Speed Optical Communications. *Nat. Photonics* **2010**, *4*, 297–301.
8. Zhang, Y.; Liu, T.; Meng, B.; Li, X.; Liang, G.; Hu, X.; Wang, Q. J. Broadband High Photoresponse from Pure Monolayer Graphene Photodetector. *Nat. Commun.* **2013**, *4*, 1811.
9. Xia, F.; Mueller, T.; Lin, Y.-m.; Valdes-Garcia, A.; Avouris, P. Ultrafast Graphene Photodetector. *Nat. Nanotechnol.* **2009**, *4*, 839–843.
10. Pesin, D.; MacDonald, A. H. Spintronics and Pseudospintronics in Graphene and Topological Insulators. *Nat. Mater.* **2012**, *11*, 409–416.
11. Shi, Z.; Jin, C.; Yang, W.; Ju, L.; Horng, J.; Lu, X.; Bechtel, H. A.; Martin, M. C.; Fu, D.; Wu, J. Gate-Dependent Pseudospin Mixing in Graphene/Boron Nitride Moiré Superlattices. *Nat. Phys.* **2014**, *10*, 743–747.
12. Hong, S. S.; Cha, J. J.; Kong, D.; Cui, Y. Ultra-Low Carrier Concentration and Surface-Dominant Transport in Antimony-Doped Bi_2Se_3 Topological Insulator Nanoribbons. *Nat. Commun.* **2012**, *3*, 757.
13. Wang, Z.; Sun, Y.; Chen, X.-Q.; Franchini, C.; Xu, G.; Weng, H.; Dai, X.; Fang, Z. Dirac Semimetal and Topological Phase Transitions in A_3Bi (a= Na, K, Rb). *Phys. Rev. B: Condens. Matter Mater. Phys.* **2012**, *85*, 195320.
14. Wang, Z.; Weng, H.; Wu, Q.; Dai, X.; Fang, Z. Three-Dimensional Dirac Semimetal and Quantum Transport in Cd_3As_2. *Phys. Rev. B: Condens. Matter Mater. Phys.* **2013**, *88*, 125427.
15. Young, S. M.; Zaheer, S.; Teo, J. C.; Kane, C. L.; Mele, E. J.; Rappe, A. M. Dirac Semimetal in Three Dimensions. *Phys. Rev. Lett.* **2012**, *108*, 140405.
16. Yang, B.-J.; Nagaosa, N. Classification of Stable Three-Dimensional Dirac Semimetals with Nontrivial Topology. *Nat. Commun.* **2014**, *5*, 4898.
17. Ezawa, M. Spin Valleytronics in Silicene: Quantum Spin Hall−Quantum Anomalous Hall Insulators and Single-Valley Semimetals. *Phys. Rev. B: Condens. Matter Mater. Phys.* **2013**, *87*, 155415.
18. Borisenko, S.; Gibson, Q.; Evtushinsky, D.; Zabolotnyy, V.; Büchner, B.; Cava, R. J. Experimental Realization of a Three-Dimensional Dirac Semimetal. *Phys. Rev. Lett.* **2014**, *113*, 027603.
19. Neupane, M.; Xu, S.-Y.; Sankar, R.; Alidoust, N.; Bian, G.; Liu, C.; Belopolski, I.; Chang, T.-R.; Jeng, H.-T.; Lin, H. Observation of a Three-Dimensional Topological Dirac Semimetal Phase in High-Mobility Cd_3As_2. *Nat. Commun.* **2014**, *5*, 3786.

20. Liu, Z.; Jiang, J.; Zhou, B.; Wang, Z.; Zhang, Y.; Weng, H.; Prabhakaran, D.; Mo, S.; Peng, H.; Dudin, P. A Stable Three-Dimensional Topological Dirac Semimetal Cd_3As_2. *Nat. Mater.* **2014**, *13*, 677–681.
21. Jeon, S.; Zhou, B. B.; Gyenis, A.; Feldman, B. E.; Kimchi, I.; Potter, A. C.; Gibson, Q. D.; Cava, R. J.; Vishwanath, A.; Yazdani, A. Landau Quantization and Quasiparticle Interference in the Three-Dimensional Dirac Semimetal Cd_3As_2. *Nat. Mater.* **2014**, *13*, 851–856.
22. Zdanowicz, W.; Zdanowicz, L. Semiconducting Compounds of the Aii Bv Group. *Annu. Rev. Mater. Sci.* **1975**, *5*, 301–328.
23. Liang, T.; Gibson, Q.; Ali, M. N.; Liu, M.; Cava, R.; Ong, N. Ultrahigh Mobility and Giant Magnetoresistance in the Dirac Semimetal Cd_3As_2. *Nat. Mater.* **2015**, *14*, 280–284.
24. Feng, J.; Pang, Y.; Wu, D.; Wang, Z.; Weng, H.; Li, J.; Dai, X.; Fang, Z.; Shi, Y.; Lu, L. Large Linear Magnetoresistance in Dirac Semi-Metal Cd_3As_2 with Fermi Surfaces Close to the Dirac Points. **2014**, *arXiv:1405.6611*.
25. He, L.; Hong, X.; Dong, J.; Pan, J.; Zhang, Z.; Zhang, J.; Li, S. Quantum Transport Evidence for the Three-Dimensional Dirac Semimetal Phase in Cd_3As_2. *Phys. Rev. Lett.* **2014**, *113*, 246402.
26. Aggarwal, L.; Gaurav, A.; Thakur, G. S.; Haque, Z.; Ganguli, A. K.; Sheet, G. Unconventional Superconductivity at Mesoscopic Point-Contacts on the 3-Dimensional Dirac Semi-Metal Cd_3As_2. **2014**, *arXiv:1410.2072*.
27. Wang, H.; Wang, H.; Liu, H.; Lu, H.; Jia, S.; Liu, X.-J.; Xie, X.; Wei, J.; Wang, J. Discovery of Superconductivity in 3D Dirac Semimetal Cd_3As_2 Crystal. **2015**, *arXiv:1501.00418*.
28. Rosenstein, B.; Shapiro, B. Y.; Shapiro, I. Ginzburg-Landau Theory of the Triplet Superconductivity in 3D Dirac Semi-Metal. **2015**, *arXiv:1501.07910*.
29. He, L.; Jia, Y.; Zhang, S.; Hong, X.; Jin, C.; Li, S. Pressure-Induced Superconductivity in the Three-Dimensional Dirac Semimetal Cd_3as_2. **2015**, *arXiv:1502.02509*.
30. Omari, M.; Kouklin, N.; Lu, G.; Chen, J.; Gajdardziska-Josifovska, M. Fabrication of Cd_3As_2 Nanowires by Direct Vapor−Solid Growth, and Their Infrared Absorption Properties. *Nanotechnology* **2008**, *19*, 105301.
31. Schönherr, P.; Hesjedal, T. Structural Properties and Growth Mechanism of Cd_3As_2 Nanowires. *Appl. Phys. Lett.* **2015**, *106*, 013115.
32. Sierański, K.; Szatkowski, J.; Misiewicz, J. Semiempirical Tight-Binding Band Structure of Ii_3V_2 Semiconductors: Cd_3P_2, Zn_3P_2, Cd_3As_2, and Zn_3As_2. *Phys. Rev. B: Condens. Matter Mater. Phys.* **1994**, *50*, 7331.
33. Han, M. Y.; Özyilmaz, B.; Zhang, Y.; Kim, P. Energy Band-Gap Engineering of Graphene Nanoribbons. *Phys. Rev. Lett.* **2007**, *98*, 206805.
34. Balog, R.; Jørgensen, B.; Nilsson, L.; Andersen, M.; Rienks, E.; Bianchi, M.; Fanetti, M.; Lægsgaard, E.; Baraldi, A.; Lizzit, S. Bandgap Opening in Graphene Induced by Patterned Hydrogen Adsorption. *Nat. Mater.* **2010**, *9*, 315–319.
35. Liao, Z.-M.; Han, B.-H.; Zhou, Y.-B.; Yu, D.-P. Hysteresis Reversion in Graphene Field-Effect Transistors. *J. Chem. Phys.* **2010**, *133*, 044703.
36. Wang, D.; Wang, Q.; Javey, A.; Tu, R.; Dai, H.; Kim, H.; McIntyre, P. C.; Krishnamohan, T.; Saraswat, K. C. Germanium Nanowire Field-Effect Transistors with SiO_2 and High-K HfO_2 Gate Dielectrics. *Appl. Phys. Lett.* **2003**, *83*, 2432.
37. Ford, A. C.; Ho, J. C.; Chueh, Y.-L.; Tseng, Y.-C.; Fan, Z.; Guo, J.; Bokor, J.; Javey, A. Diameter-Dependent Electron Mobility of Inas Nanowires. *Nano Lett.* **2009**, *9*, 360–365.
38. Javey, A.; Kim, H.; Brink, M.; Wang, Q.; Ural, A.; Guo, J.; McIntyre, P.; McEuen, P.; Lundstrom, M.; Dai, H. High-Kappa Dielectrics for Advanced Carbon-Nanotube Transistors and Logic Gates. *Nat. Mater.* **2002**, *1*, 241–6.
39. Lin, Y.-M.; Cronin, S. B.; Ying, J. Y.; Dresselhaus, M.; Heremans, J. P. Transport Properties of Bi Nanowire Arrays. *Appl. Phys. Lett.* **2000**, *76*, 3944–3946.
40. Radisavljevic, B.; Kis, A. Mobility Engineering and a Metal-Insulator Transition in Monolayer MoS_2. *Nat. Mater.* **2013**, *12*, 815–820.
41. Zdanowicz, L.; Portal, J.; Zdanowicz, W. Shubnikov-De Haas Effect in Amorphous Cd_3As_2. *Lect. Notes Phys.* **1983**, *177*, 386–395.
42. Xiang, F.-X.; Wang, X.-L.; Veldhorst, M.; Dou, S.-X.; Fuhrer, M. S. Observation of Topological Transition of Fermi Surface from a Spindle-Torus to a Torus in Large Bulk Rashba Spin-Split Bitecl. **2015**, *arXiv:1501.03240*.
43. Murakawa, H.; Bahramy, M.; Tokunaga, M.; Kohama, Y.; Bell, C.; Kaneko, Y.; Nagaosa, N.; Hwang, H.; Tokura, Y. Detection of Berry's Phase in a Bulk Rashba Semiconductor. *Science* **2013**, *342*, 1490–1493.
44. Zhao, Y.; Liu, H.; Zhang, C.; Wang, H.; Wang, J.; Lin, Z.; Xing, Y.; Lu, H.; Liu, J.; Wang, Y. Anomalous Quantum Oscillations in 3D Dirac Semimetal Cd_3As_2 Induced by 3D Nested Anisotropic Fermi Surface. **2014**, *arXiv:1412.0330*.
45. Pariari, A.; Dutta, P.; Mandal, P. Probing the Fermi Surface of 3D Dirac Semimetal Cd_3As_2 through De Haas-Van Alphen Technique. **2015**, *arXiv:1501.01175*.
46. Narayanan,A.; Watson, M.; Blake, S.; Chen, Y.; Prabhakaran, D.; Yan, B.; Bruyant, N.; Drigo, L.; Mazin, I.; Felser, C. Linear Magnetoresistance Caused by Mobility Fluctuations in the N-Doped Cd_3As_2. **2014**, *arXiv:1412.4105*.
47. Lee, S.; In, J.; Yoo, Y.; Jo, Y.; Park, Y. C.; Kim, H.-j.; Koo, H. C.; Kim, J.; Kim, B.; Wang, K. L. Single Crystalline B-Ag_2Te Nanowire as a New Topological Insulator. *Nano Lett.* **2012**, *12*, 4194–4199.
48. Qu, D.-X.; Hor, Y.; Xiong, J.; Cava, R.; Ong, N. Quantum Oscillations and Hall Anomaly of Surface States in the Topological Insulator Bi_2Te_3. *Science* **2010**, *329*, 821–824.
49. Analytis, J. G.; McDonald, R. D.; Riggs, S. C.; Chu, J.-H.; Boebinger, G.; Fisher, I. R. Two-Dimensional Surface State in the Quantum Limit of a Topological Insulator. *Nat. Phys.* **2010**, *6*, 960–964.
50. Li, L.; Ye, G. J.; Tran, V.; Fei, R.; Chen, G.; Wang, H.; Wang, J.; Watanabe, K.; Taniguchi, T.; Yang, L. Quantum Oscillations in Black Phosphorus Two-Dimensional Electron Gas. **2014**, *arXiv:1411.6572*
51. Gehring, P.; Gao, B. F.; Burghard, M.; Kern, K. Growth of High-Mobility Bi_2Te_2Se Nanoplatelets on Hbn Sheets by Van Der Waals Epitaxy. *Nano Lett.* **2012**, *12*, 5137–5142.
52. Wang, Y.; Xiu, F.; Cheng, L.; He, L.; Lang, M.; Tang, J.; Kou, X.; Yu, X.; Jiang, X.; Chen, Z. Gate-Controlled Surface Conduction in Na-Doped Bi_2Te_3 Topological Insulator Nanoplates. *Nano Lett.* **2012**, *12*, 1170–1175.